EUROPEAN ORGANIZATION FOR NUCLEAR RESEARCH (CERN)

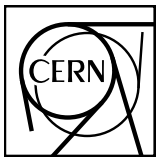

CERN-EP-2023-007
26 January 2023

Measurement of the $\Lambda_b^0 \to \Lambda(1520)\mu^+\mu^-$ differential branching fraction

LHCb collaboration

Abstract

The branching fraction of the rare decay $\Lambda_b^0 \to \Lambda(1520)\mu^+\mu^-$ is measured for the first time, in the squared dimuon mass intervals, q^2, excluding the J/ψ and $\psi(2S)$ regions. The data sample analyzed was collected by the LHCb experiment at center-of-mass energies of 7, 8, and 13 TeV, corresponding to a total integrated luminosity of $9\,\text{fb}^{-1}$. The result in the highest q^2 interval, $q^2 > 15.0\,\text{GeV}^2/c^4$, where theoretical predictions have the smallest model dependence, agrees with the predictions.

Submitted to Phys. Rev. Lett.

The Standard Model (SM) of particle physics provides at present the best description of fundamental particles and their interactions. However, it is unable to explain the dominance of matter over antimatter or the patterns of the interaction strengths of the elementary particles. Physics beyond the SM (BSM) is needed to address these limitations.

One way of searching for BSM physics is to study the flavor changing neutral-current (FCNC) transition $b \to s\ell^+\ell^-$, which proceeds through electroweak loop diagrams in the SM, while a sizeable contribution could be introduced by BSM physics [1–3]. Such decays have been studied in the B-meson sector by measuring branching fractions [4–7], angular distributions [8–13] and testing lepton flavor universality (LFU) [14–20]. Similar to B-meson decays, the study of B-baryon decays offers a multitude of observables that are analogous to those typically measured in B-meson decays, including charge-parity (CP) asymmetries. Due to the half-integer spin, the B-baryon decays offer an even richer angular structure than the B-meson decays [21].

The differential branching fraction and angular observables of the $\Lambda_b^0 \to \Lambda\mu^+\mu^-$ decay were analyzed by the LHCb collaboration [22], and the measured values can be described by recent theoretical calculations [23, 24]. The $\Lambda_b^0 \to pK^-\mu^+\mu^-$ decay was first observed by the LHCb collaboration [25], and a search for CP violation was performed. A test of lepton flavor universality in the decay $\Lambda_b^0 \to pK^-\ell^+\ell^-$ was carried out by the LHCb collaboration [26], and the result was found to be consistent with SM predictions. In the aforementioned measurements, there are various contributions of excited Λ baryon resonances to the pK^- final state, among which the $\Lambda(1520)$ stands out as having a relatively narrow width of 16 MeV [27]. In contrast to the ground state Λ, which has a spin parity of $J^P = (1/2)^-$, the excited $\Lambda(1520)$ state has a spin parity of $J^P = (3/2)^-$, providing complementary information on potential new physics effects in the $b \to s\ell^+\ell^-$ transitions [28].

This Letter reports the first measurement of the differential branching fraction of the $\Lambda_b^0 \to \Lambda(1520)\mu^+\mu^-$ decay in intervals of the squared dimuon mass, q^2, with the $\Lambda(1520)$ baryon reconstructed through its $\Lambda(1520) \to pK^-$ decay. The inclusion of charge-conjugate processes is implied throughout this Letter. The more abundant tree-level decay $\Lambda_b^0 \to pK^-J/\psi$, with a well-measured branching fraction [29], is used for normalization. The measurements are performed using proton-proton (pp) collision data corresponding to an integrated luminosity of $9\,\text{fb}^{-1}$ recorded by the LHCb experiment at center-of-mass energies of 7, 8 and 13 TeV.

The LHCb detector [30, 31] is a single-arm forward spectrometer covering the pseudorapidity range $2 < \eta < 5$, designed for the study of particles containing b or c quarks. The online event selection is performed by a trigger [32, 33], which consists of a hardware stage, based on information from the calorimeters and muon systems [34], followed by a software stage, which applies a full event reconstruction. Simulated events are used to develop the candidate selection and to estimate the corresponding efficiency for the signal and normalization modes. In the simulation, pp collisions are generated using Pythia 8 [35] with a specific LHCb configuration [36]. Decays of unstable particles are described by EvtGen [37], in which final-state radiation is generated using Photos [38]. The interaction of the generated particles with the detector, and its response, are simulated using the Geant4 toolkit [39] as described in Ref. [40]. The $\Lambda_b^0 \to \Lambda(1520)\mu^+\mu^-$ and $\Lambda_b^0 \to pK^-J/\psi$ decays are simulated following a uniform phase-space model, and the intermediate resonant structures in the $\Lambda_b^0 \to pK^-J/\psi$ decay are corrected based on the amplitude analysis in Ref. [41]. The Λ_b^0 lifetime in the simulation is corrected to its known

value [29]. In addition, the detector occupancy and Λ_b^0 transverse momentum, $p_{\rm T}(\Lambda_b^0)$, distributions of all simulated samples involving Λ_b^0 decays are corrected for discrepancies between the simulation and data, using $\Lambda_b^0 \to pK^-J/\psi$ samples.

Candidate $\Lambda(1520)$ baryon decays are reconstructed from two oppositely charged tracks identified as a proton and a kaon originating from a common vertex. No requirement on the $m(pK^-)$ mass is applied. The $\Lambda_b^0 \to \Lambda(1520)(\to pK^-)\mu^+\mu^-$ decay is reconstructed by combining a $\Lambda(1520)$ candidate with two oppositely charged tracks identified as muons. Dimuon pairs having mass squared q^2 values around the J/ψ ($8.0 < q^2 < 11.0\,{\rm GeV}^2/c^4$) and $\psi(2S)$ ($12.5 < q^2 < 15.0 <$ ${\rm GeV}^2/c^4$) resonances are vetoed from the signal decay sample, while the candidates from the $\Lambda_b^0 \to pK^-J/\psi$ decay are used for normalization. The background is further suppressed by requirements on the quality of the Λ_b^0 decay vertex, the flight distance significance of the Λ_b^0 candidate, the compatibility of the Λ_b^0 candidate to come from the primary pp interaction vertex (PV), and the separation of the final-state tracks from the PV. For the $\Lambda_b^0 \to pK^-J/\psi$ decay, the mass of the Λ_b^0 candidate is recalculated with the J/ψ meson mass constrained to its known value [29], leading to an improvement on the Λ_b^0 mass resolution.

Various vetoes on hadron and muon masses reject peaking backgrounds originating from misidentified b-hadron decays, by recalculating the mass of the four-track combination under alternative particle hypotheses and removing candidates in the relevant mass range. Background candidates in the $\Lambda_b^0 \to \Lambda(1520)(\to pK^-)\mu^+\mu^-$ sample can originate from a few different sources. These include the $B_s^0 \to \phi(1020)(\to K^+K^-)\mu^+\mu^-$ decay, where a kaon is misidentified as a proton; contamination from $B^- \to K^-\mu^+\mu^-$ decays combined with a random additional proton; and the $\Lambda_b^0 \to pD^0(\to K^-\pi^+)\pi^-$ decay, where both pions are misidentified as muons. The same vetoes on the B_s^0 and B^- decays are used to reject backgrounds in the $\Lambda_b^0 \to pK^-J/\psi$ data sample. Due to the narrow J/ψ mass window requirement, the $\Lambda_b^0 \to pD^0(\to K^-\pi^+)\pi^-$ background is negligible for the $\Lambda_b^0 \to pK^-J/\psi$ decay, and therefore the veto is not applied. The J/ψ contamination in the signal decay sample with a muon misidentified as a hadron is found to be negligible. These vetoes retain about 91% of the signal while strongly suppressing all these background sources. The background from $\Lambda_b^0 \to \Lambda_c^+(\to pK^-X)Y$ decays, where X and Y can represent either a $\mu^-\overline{\nu}_\mu$ ($\mu^+\nu_\mu$) pair or a pion, are verified to be negligible in the $\Lambda_b^0 \to \Lambda(1520)(\to pK^-)\mu^+\mu^-$ signal sample.

In order to increase the signal purity, a multivariate classification is employed using a Boosted Decision Tree (BDT) [42, 43] algorithm implemented in the TMVA package [44]. To train this classifier, simulated $\Lambda_b^0 \to \Lambda(1520)(\to pK^-)\mu^+\mu^-$ candidates are used as the signal proxy, and candidates lying in the upper $pK^-\mu^+\mu^-$ mass sideband (6.0–6.8 ${\rm GeV}/c^2$) adjacent to the signal region are used as background proxy. The variables used in the BDT training include kinematical and topological properties of the final state or intermediate particles. The requirement on the multivariate output is optimized by maximizing the magnitude of $N_{\rm S}/\sqrt{N_{\rm S}+N_{\rm B}}$, where $N_{\rm S}$ and $N_{\rm B}$ are the expected number of $\Lambda_b^0 \to \Lambda(1520)\mu^+\mu^-$ signal and background candidates underneath the signal peak, respectively. The same BDT selection is applied to the $\Lambda_b^0 \to pK^-J/\psi$ normalization mode.

With the full selection applied, the differential branching fraction of the $\Lambda_b^0 \to \Lambda(1520)\mu^+\mu^-$ decay is determined in intervals of q^2, relative to the $\Lambda_b^0 \to pK^-J/\psi$

normalization mode, according to

$$\left[\frac{d\mathcal{B}(\Lambda_b^0 \to \Lambda(1520)\mu^+\mu^-)}{dq^2}\right]_{q^2_{\rm min}}^{q^2_{\rm max}} = \frac{1}{(q^2_{\rm max} - q^2_{\rm min})} \frac{\mathcal{B}(\Lambda_b^0 \to pK^-J/\psi)\mathcal{B}(J/\psi \to \mu^+\mu^-)}{\mathcal{B}(\Lambda(1520) \to pK^-)} \times \frac{N_{\Lambda(1520)\mu^+\mu^-}}{N_{pK^-J/\psi}} \frac{\varepsilon_{pK^-J/\psi}}{\varepsilon_{\Lambda(1520)\mu^+\mu^-}}, \quad (1)$$

where $N_{pK^-J/\psi}$ and $\varepsilon_{pK^-J/\psi}$ are the yields and efficiencies of the normalization mode, and $N_{\Lambda(1520)\mu^+\mu^-}$ and $\varepsilon_{\Lambda(1520)\mu^+\mu^-}$ indicate the corresponding parameters for the signal mode in the $q^2_{\rm min}$–$q^2_{\rm max}$ interval. The branching fractions $\mathcal{B}(\Lambda_b^0 \to pK^-J/\psi)$, $\mathcal{B}(J/\psi \to \mu^+\mu^-)$ and $\mathcal{B}(\Lambda(1520) \to pK^-)$ are $(3.2 \pm 0.6) \times 10^{-4}$, (5.961±0.033)% and (22.5 ± 0.5)%, respectively [29].

To determine the geometrical acceptance and the efficiencies of the trigger, reconstruction, and particle identification (PID) requirements, we utilize the simulation and apply corrections based on unbiased control samples selected from real data. These corrections are applied to simulated samples of the signal and normalization modes to refine their accuracy. The PID efficiencies for each channel are calculated from calibration data samples of muons, proton, kaons and pions [45], and are applied as per-candidate weights to the simulation. Similarly, the trigger efficiency is corrected by comparing the efficiency in data and simulation as a function of the $p_{\rm T}$ of the muons in the normalization mode. Finally, the relative efficiencies for different data-taking periods are combined according to the integrated luminosity times the production rate of the Λ_b^0 baryon to account for the variation of data-taking conditions.

The yield of the $\Lambda_b^0 \to pK^-J/\psi$ normalization mode is determined using an extended unbinned maximum-likelihood fit to the pK^-J/ψ mass distribution with the J/ψ meson mass constrained to its known value [29]. The signal is modelled by a Hypatia function [46]. The tail parameters are determined from simulation, while the peak position and resolution are allowed to vary freely in the fit to data. The combinatorial background is modelled using an exponential function with the slope allowed to vary freely. The $m(pK^-\mu^+\mu^-)$ distribution of the selected $\Lambda_b^0 \to pK^-J/\psi$ candidates is shown in Fig. 1 (left), with the fit results overlaid. The $\Lambda_b^0 \to pK^-J/\psi$ yield is found to be $N_{pK^-J/\psi} = 137\,900 \pm 405$, where the uncertainty is statistical only.

For the $\Lambda_b^0 \to \Lambda(1520)\mu^+\mu^-$ decay, we perform a simultaneous extended unbinned maximum-likelihood fit to the $pK^-\mu^+\mu^-$ mass distribution in different intervals of q^2. The mean of the signal peak is shared among the different samples. The same signal and background models as for the $\Lambda_b^0 \to pK^-J/\psi$ normalization mode are used, while the tail parameters of the signal model are determined from the simulated $\Lambda_b^0 \to \Lambda(1520)\mu^+\mu^-$ sample. The $m(pK^-\mu^+\mu^-)$ resolution parameter for the signal component is fixed to the value obtained from a fit to the normalization mode. Figure 1 (right) shows the $m(pK^-\mu^+\mu^-)$ distribution of the full data sample, integrated over all the considered q^2 intervals. The $\Lambda_b^0 \to pK^-\mu^+\mu^-$ signal yield is found to be $N_{\Lambda_b^0 \to pK^-\mu^+\mu^-} = 2\,250 \pm 57$, where the uncertainty is statistical only. The corresponding figures for all the q^2 ranges are available as Supplemental Material [47].

The yields of the $\Lambda_b^0 \to \Lambda(1520)\mu^+\mu^-$ signal in the different q^2 bins are determined by maximizing the extended weighted log-likelihood for unbinned $m(pK^-)$ distributions. The non-Λ_b^0 background is subtracted using the *sPlot* technique, which utilizes the $m(pK^-\mu^+\mu^-)$ distribution as a discriminating variable [48, 49]. The fit procedure is validated with

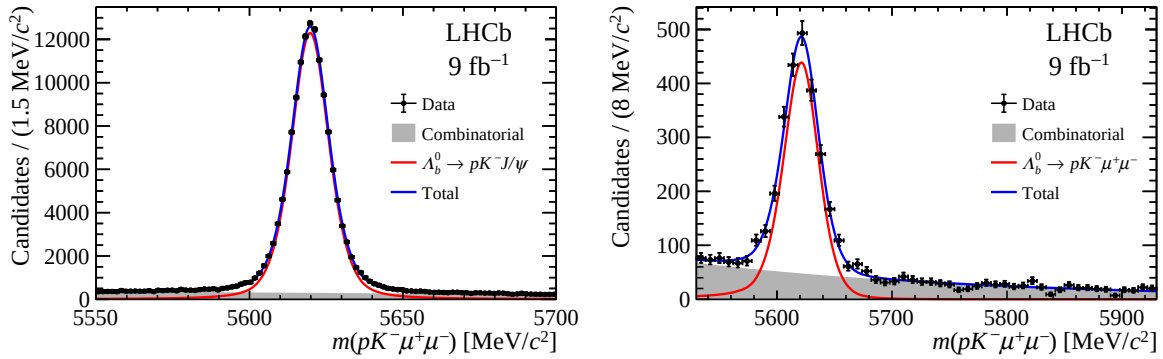

Figure 1: Mass distribution for the (left) $\Lambda_b^0 \to pK^- J/\psi$ and (right) $\Lambda_b^0 \to pK^-\mu^+\mu^-$, integrated over the considered q^2 intervals. Fit results are overlaid.

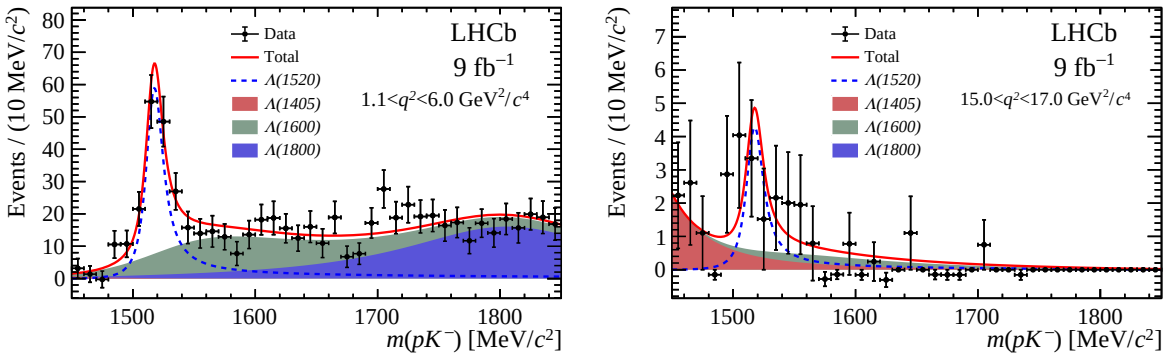

Figure 2: Distribution of the pK^- mass, after background subtraction, for $\Lambda_b^0 \to \Lambda(1520)\mu^+\mu^-$ signal candidates in the (left) $1.1 < q^2 < 6.0\,\text{GeV}^2/c^4$ and (right) $15.0 < q^2 < 17.0\,\text{GeV}^2/c^4$ regions. Fit results are overlaid.

pseudoexperiments, and the uncertainties of the $\Lambda_b^0 \to \Lambda(1520)\mu^+\mu^-$ signal yields are corrected using the bootstrap method [50]. A cross-check is performed using unbinned maximum-likelihood fits to the two-dimensional $m(pK^-\mu^+\mu^-)$ and $m(pK^-)$ distributions, which give consistent results. Considering the mass and width of all the Λ states [29] and their contributions to the background-subtracted $m(pK^-)$ spectra, the $\Lambda(1405)$, $\Lambda(1520)$, $\Lambda(1600)$ and $\Lambda(1800)$ states are included in the nominal fits. The lineshapes of these resonances are parameterized using relativistic Breit–Wigner functions. The efficiency as a function of $m(pK^-)$ is determined from simulation and included in the fit model. As the $\Lambda(1520)$ resonance has a width that is comparable to the experimental resolution, the lineshape is convolved with a Gaussian resolution function. The width of the Gaussian is taken from the simulation. In the fits to the background-subtracted $m(pK^-)$ distributions, the width and mass of all the Λ resonances are fixed according to the world's best results [27, 51]. The $\Lambda(1670), \Lambda(1690), \Lambda(1820), \Lambda(1830)$ states, and interference effects are not included in the fits as these are found to be small, and a systematic uncertainty is included in that of the signal fit mode. The background-subtracted $m(pK^-)$ distribution in the q^2 regions 1.1–6.0 GeV^2/c^4 and 15.0–17.0 GeV^2/c^4 are shown in Fig. 2. The signal yields in all the q^2 intervals are given in Table 2.

The differential branching fraction measurement is affected by systematic uncertainties

Table 1: Relative systematic uncertainties [in %] of the differential branching fraction ratio measurement. The total uncertainty is obtained as the quadratic sum of the individual contributions.

Source	q^2 interval [GeV$^2/c^4$]					
	0.1–3.0	3.0–6.0	6.0–8.0	11.0–12.5	15.0–17.0	1.1–6.0
Signal fit model	9.6	6.5	9.3	9.3	15.3	7.2
Normalization fit model	1.3	1.3	1.3	1.3	1.3	1.3
Hardware trigger	0.3	0.5	0.2	0.1	0.1	0.3
PID	2.4	2.4	1.6	7.0	16.0	2.4
Simulation corrections	0.1	0.1	0.1	0.1	0.1	0.1
Decay model	1.7	2.6	4.8	4.0	5.4	0.9
Simulated sample size	0.2	0.2	0.2	0.3	0.5	0.1
$\mathcal{B}(J/\psi \to \mu^+\mu^-)/\mathcal{B}(\Lambda(1520) \to pK^-)$	2.3	2.3	2.3	2.3	2.3	2.3
Quadratic sum	10.4	7.9	10.9	12.6	22.9	8.1
$\mathcal{B}(\Lambda_b^0 \to pK^-J/\psi)$	18.8	18.8	18.8	18.8	18.8	18.8

in the yield determination and the efficiency estimation. Table 1 lists these systematic uncertainties. The total uncertainty is determined from the sum of all contributions in quadrature. The largest uncertainty is related to the uncertainty on the measured mass and width of the Λ resonances that are fixed in the signal fit model, and is estimated using pseudoexperiments. Pseudodata samples are generated according to an alternative model in which the mass and width of the Λ resonances are varied within their uncertainty [27,51], and input values for the Blatt-Weisskopf barrier functions [52] of the Λ resonances are varied, then fitted with the default model.

The systematic uncertainty of the Λ_b^0 yield determination is evaluated using pseudoexperiments. For both the signal mode $\Lambda_b^0 \to \Lambda(1520)\mu^+\mu^-$ and the $\Lambda_b^0 \to pK^-J/\psi$ normalization mode, an alternative model is used where the signal is described by a double-sided Crystal Ball function [53] and the background by a second-order Chebyshev polynomial function [54]. Pseudosamples are generated using the alternative model and fitted with the default model, and the observed deviation is assigned as the systematic uncertainty. Peaking backgrounds that remain after the vetoes introduced in the selection are neglected in the fit for the determination of the $\Lambda_b^0 \to pK^-J/\psi$ yield. The main sources of systematic uncertainty are caused by contributions from the $B_s^0 \to K^+K^-J/\psi$ and $B^0 \to K^+\pi^-J/\psi$ decays.

The hardware-trigger efficiencies are measured in bins of muon $p_{\rm T}$ using the $\Lambda_b^0 \to pK^-J/\psi$ data sample. The effect of an alternative binning scheme on the efficiency ratio is taken as a systematic uncertainty. The PID efficiency is determined in bins of the particle momentum and pseudorapidity using calibration data samples. The effects of different binning schemes and different calibration samples are evaluated. The sum in quadrature of these effects is taken as the systematic uncertainty arising from the PID efficiency.

The systematic uncertainty associated with the simulation corrections is determined by using alternative binning schemes to account for the finite statistics of the control modes. The corresponding deviation is taken as the systematic uncertainty. The systematic uncertainty associated with the decay model used in simulation is estimated by taking the

Table 2: Signal yields and the absolute differential branching fraction, in bins of q^2, for the $\Lambda_b^0 \to \Lambda(1520)\mu^+\mu^-$ decay. The first uncertainty is statistical, the second systematic, and the third due to the uncertainty on the $\Lambda_b^0 \to pK^-J/\psi$ and $J/\psi \to \mu^+\mu^-$ branching fractions.

q^2 interval [GeV$^2/c^4$]	$N_{\Lambda(1520)\mu^+\mu^-}$	$\frac{d\mathcal{B}(\Lambda_b^0\to\Lambda(1520)\mu^+\mu^-)}{dq^2}$ [10^{-8} GeV$^{-2}c^4$]
0.1–3.0	96 ± 18	$1.89 \pm 0.35 \pm 0.19 \pm 0.36$
3.0–6.0	138 ± 18	$2.42 \pm 0.32 \pm 0.17 \pm 0.45$
6.0–8.0	65 ± 14	$1.58 \pm 0.36 \pm 0.16 \pm 0.30$
11.0–12.5	59 ± 14	$2.07 \pm 0.47 \pm 0.26 \pm 0.39$
15.0–17.0	12 ± 5	$0.57 \pm 0.24 \pm 0.13 \pm 0.11$
1.1–6.0	175 ± 21	$1.95 \pm 0.23 \pm 0.16 \pm 0.37$

difference in efficiency between the phase-space model and the model given in Ref [55]. In addition, the systematic uncertainties due to the limited size of the simulated sample and precision of the $J/\psi \to \mu^+\mu^-$ and $\Lambda(1520) \to pK^-$ branching fractions are also taken into account.

The differential branching fraction of the $\Lambda_b^0 \to \Lambda(1520)\mu^+\mu^-$ decay in intervals of q^2 is reported in Table 2, and is shown in Fig. 3. The SM prediction from Ref. [55], for which only the form factor uncertainties are considered, and the SM prediction from Refs. [56] and [57], are also shown. It is impossible to make a firm statement about the level of

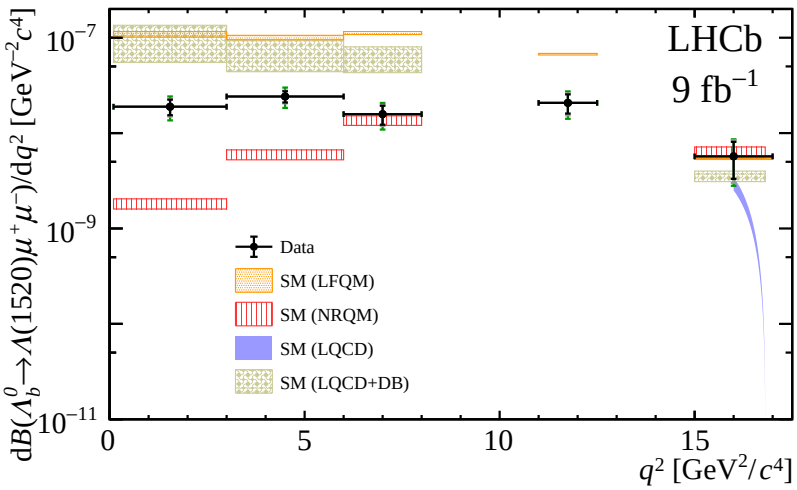

Figure 3: Differential branching fraction of the $\Lambda_b^0 \to \Lambda(1520)\mu^+\mu^-$ decay in intervals of q^2. The error bars in black, grey and green represent the measured results with statistical, systematic and $\mathcal{B}(\Lambda_b^0 \to pK^-J/\psi)$ uncertainties taken into account. Also shown are the SM predictions using the form factors calculated with the nonrelativistic quark model (NRQM) [55], light-front quark model (LFQM) [56], joint lattice QCD and dispersive bound (LQCD+DB) [57] and lattice QCD (LQCD) [58]. Note that the LQCD prediction is only available for q^2 above 16 GeV$^2/c^4$, and the trend instead of a rate average is shown.

agreement between the experimental measurement and the theoretical predictions due to the significant variation among the different theoretical predictions.

In summary, the first measurement of the branching fraction of the rare decay $\Lambda_b^0 \to \Lambda(1520)\mu^+\mu^-$ is presented using LHCb data corresponding to a total integrated luminosity of $9\,\text{fb}^{-1}$. The data are compared to several predictions within SM. In the highest q^2 interval, $q^2 > 15.0\,\text{GeV}^2/c^4$, where the predictions have the smallest model dependence, they are consistent with the data. In the low-q^2 region, it is not possible to make a statement about the agreement between this experimental result and the predictions since the variation between the different SM predictions is much larger than their quoted uncertainties.

Supplemental material

Figure 4 shows the mass distributions of the $\Lambda_b^0 \to pK^-\mu^+\mu^-$ signal candidates in the five q^2 intervals, and integrated over the first two intervals. The total fit projection (blue line) is overlaid on the data, along with the signal component (red line) and background component describing combinatorial background (grey shadow). Figure 5 shows the pK^- mass for $\Lambda_b^0 \to \Lambda(1520)\mu^+\mu^-$ signal candidates in different q^2 bins. The total fit projection (red line) is overlaid on the data along with projections of individual fit components describing: the signal (blue dashed line) and the $\Lambda(1405)$ (red), $\Lambda(1600)$ (green) and $\Lambda(1800)$ (purple) components. Figure 6 shows the comparison between data and SM predictions in the zoomed ranges of Fig. 3.

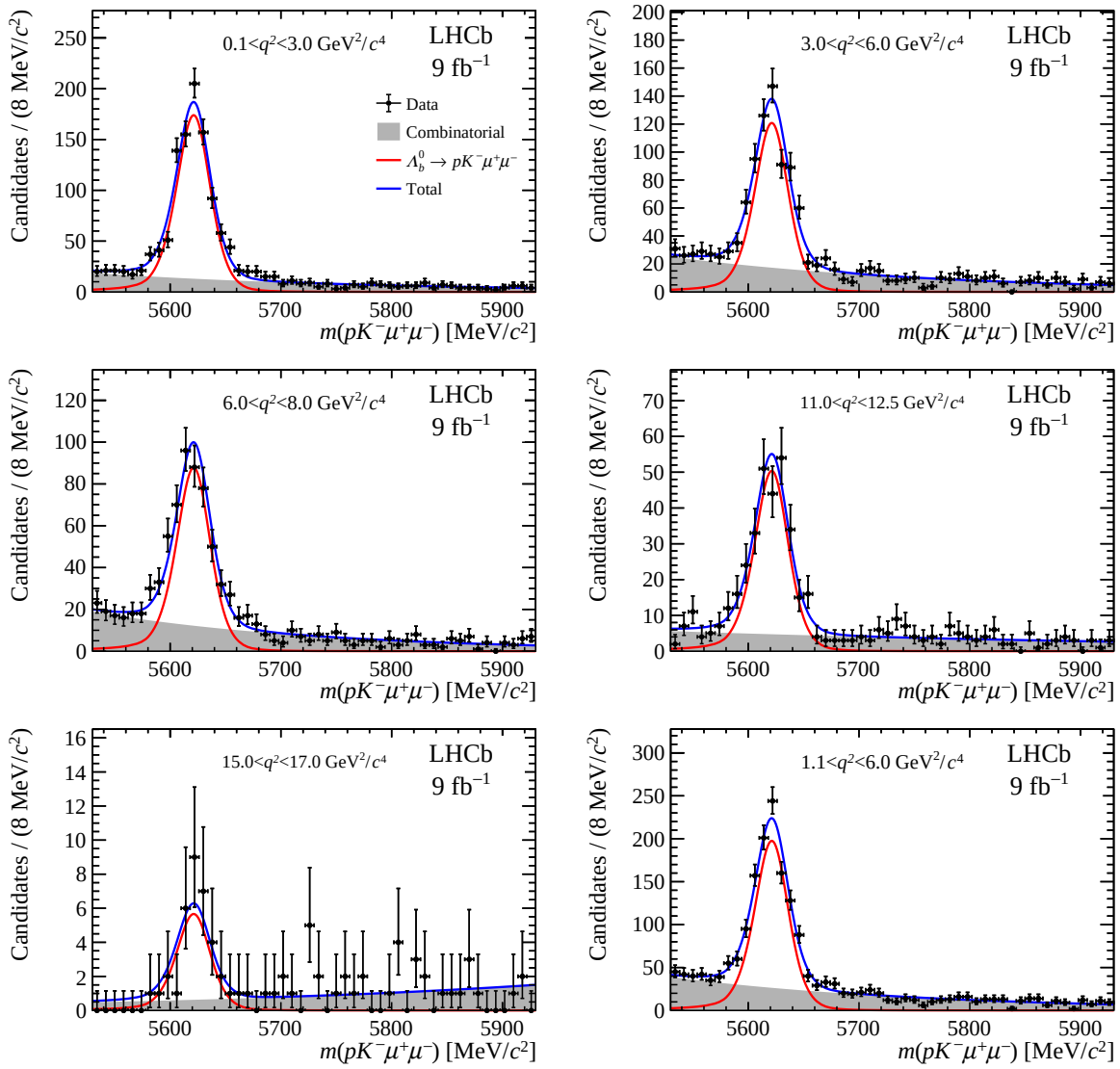

Figure 4: Mass distributions of the $\Lambda_b^0 \to pK^-\mu^+\mu^-$ signal candidates in different q^2 intervals. The data are overlaid with the fit projections.

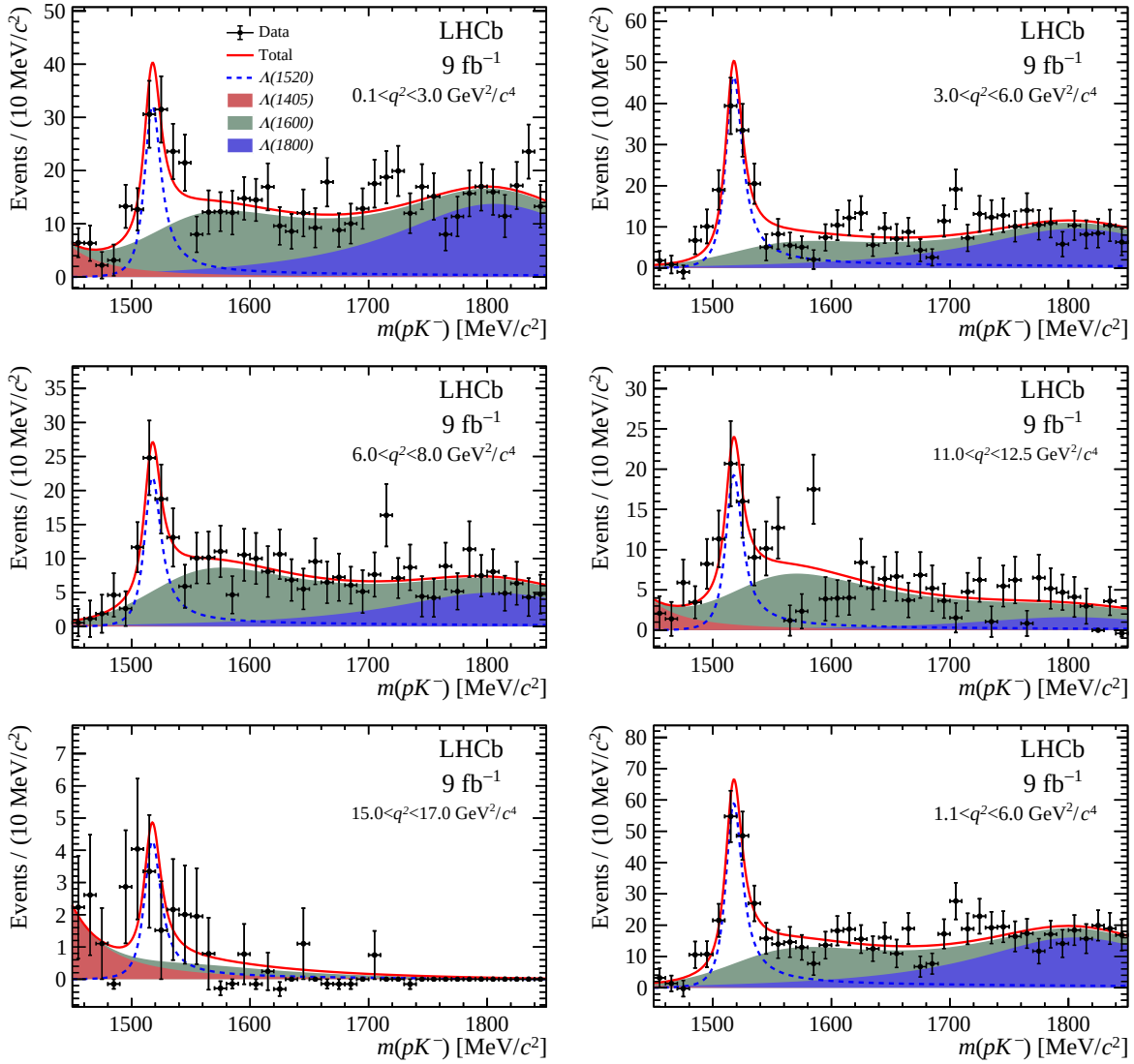

Figure 5: Distribution of pK^- mass, after background subtraction, for the $\Lambda_b^0 \to \Lambda(1520)\mu^+\mu^-$ signal candidates in intervals of q^2. Distributions are overlaid with the fit projections.

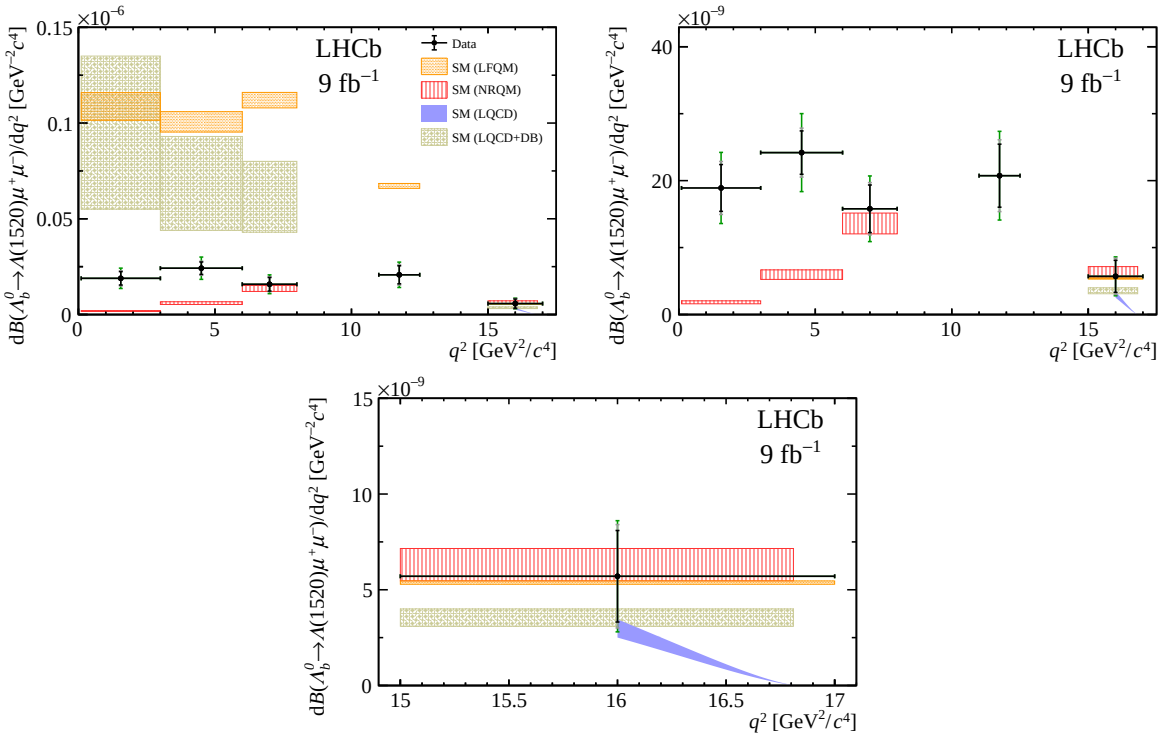

Figure 6: Comparison between data and SM predictions. Note that the LQCD prediction is only available for q^2 above 16 GeV$^2/c^4$, and the trend instead of a rate average is shown.

References

[1] D. Das, *Model independent new physics analysis in $\Lambda_b \to \Lambda\mu^+\mu^-$ decay*, Eur. Phys. J. **C78** (2018) 230, arXiv:1802.09404.

[2] P. Langacker and M. Plumacher, *Flavor changing effects in theories with a heavy Z' boson with family nonuniversal couplings*, Phys. Rev. **D62** (2000) 013006, arXiv:hep-ph/0001204.

[3] S. Biswas, S. Mahata, B. P. Nayak, and S. Sahoo, *Imprints of new physics in $\Lambda_b \to \Lambda^*\ell^+\ell^-$ decay in nonuniversal Z' model*, Int. J. Mod. Phys. **A37** (2022) 2250044.

[4] LHCb collaboration, R. Aaij *et al.*, *Measurement of the CP asymmetry in $B^+ \to K^+\mu^+\mu^-$ decays*, Phys. Rev. Lett. **111** (2013) 151801, arXiv:1308.1340.

[5] LHCb collaboration, R. Aaij *et al.*, *Differential branching fractions and isospin asymmetries of $B \to K^{(*)}\mu^+\mu^-$ decays*, JHEP **06** (2014) 133, arXiv:1403.8044.

[6] LHCb collaboration, R. Aaij *et al.*, *Measurements of the S-wave fraction in $B^0 \to K^+\pi^-\mu^+\mu^-$ decays and the $B^0 \to K^*(892)^0\mu^+\mu^-$ differential branching fraction*, JHEP **11** (2016) 047, Erratum ibid. **04** (2017) 142, arXiv:1606.04731.

[7] LHCb collaboration, R. Aaij *et al.*, *Branching fraction measurements of the rare $B_s^0 \to \phi\mu^+\mu^-$ and $B_s^0 \to f_2'(1525)\mu^+\mu^-$ decays*, Phys. Rev. Lett. **127** (2021) 151801, arXiv:2105.14007.

[8] CDF collaboration, T. Aaltonen *et al.*, *Measurements of the angular distributions in the decays $B \to K^{(*)}\mu^+\mu^-$ at CDF*, Phys. Rev. Lett. **108** (2012) 081807, arXiv:1108.0695.

[9] LHCb collaboration, R. Aaij *et al.*, *Angular analysis and differential branching fraction of the decay $B_s^0 \to \phi\mu^+\mu^-$*, JHEP **09** (2015) 179, arXiv:1506.08777.

[10] LHCb collaboration, R. Aaij *et al.*, *Angular analysis of the $B^0 \to K^{*0}\mu^+\mu^-$ decay using $3\,fb^{-1}$ of integrated luminosity*, JHEP **02** (2016) 104, arXiv:1512.04442.

[11] Belle collaboration, S. Wehle *et al.*, *Lepton-flavor-dependent angular analysis of $B \to K^*\ell^+\ell^-$*, Phys. Rev. Lett. **118** (2017) 111801, arXiv:1612.05014.

[12] LHCb collaboration, R. Aaij *et al.*, *Angular analysis of the $B^+ \to K^{*+}\mu^+\mu^-$ decay*, Phys. Rev. Lett. **126** (2021) 161802, arXiv:2012.13241.

[13] LHCb collaboration, R. Aaij *et al.*, *Angular analysis of the rare decay $B_s^0 \to \phi\mu^+\mu^-$*, JHEP **11** (2021) 043, arXiv:2107.13428.

[14] BaBar collaboration, J. P. Lees *et al.*, *Measurement of branching fractions and rate asymmetries in the rare decays $B \to K^{(*)}l^+l^-$*, Phys. Rev. **D86** (2012) 032012, arXiv:1204.3933.

[15] LHCb collaboration, R. Aaij *et al.*, *Search for lepton-universality violation in $B^+ \to K^+\ell^+\ell^-$ decays*, Phys. Rev. Lett. **122** (2019) 191801, arXiv:1903.09252.

[16] Belle collaboration, S. Choudhury *et al.*, *Test of lepton flavor universality and search for lepton flavor violation in $B \to K\ell\ell$ decays*, JHEP **03** (2021) 105, arXiv:1908.01848.

[17] Belle collaboration, A. Abdesselam *et al.*, *Test of lepton-flavor universality in $B \to K^*\ell^+\ell^-$ decays at Belle*, Phys. Rev. Lett. **126** (2021) 161801, arXiv:1904.02440.

[18] LHCb collaboration, R. Aaij *et al.*, *Tests of lepton universality using $B^0 \to K^0_S\ell^+\ell^-$ and $B^+ \to K^{*+}\ell^+\ell^-$ decays*, Phys. Rev. Lett. **128** (2022) 191802, arXiv:2110.09501.

[19] LHCb collaboration, *Test of lepton universality in $b \to s\ell^+\ell^-$ decays*, arXiv:2212.09152.

[20] LHCb collaboration, *Measurement of lepton universality parameters in $B^+ \to K^+\ell^+\ell^-$ and $B^0 \to K^{*0}\ell^+\ell^-$ decays*, arXiv:2212.09153.

[21] T. Feldmann, *Theory: Angular Distributions in Rare B Decays*, PoS **BEAUTY2020** (2021) 018, arXiv:2101.04314.

[22] LHCb collaboration, R. Aaij *et al.*, *Differential branching fraction and angular analysis of $\Lambda_b^0 \to \Lambda\mu^+\mu^-$ decays*, JHEP **06** (2015) 115, Erratum ibid. **09** (2018) 145, arXiv:1503.07138.

[23] W. Detmold and S. Meinel, *$\Lambda_b^0 \to \Lambda\ell^+\ell^-$ form factors, differential branching fraction, and angular observables from lattice QCD with relativistic b quarks*, Phys. Rev. **D93** (2016) 074501, arXiv:1602.01399.

[24] T. Blake, S. Meinel, and D. van Dyk, *Bayesian analysis of $b \to s\mu^+\mu^-$ Wilson coefficients using the full angular distribution of $\Lambda_b^0 \to \Lambda(\to p\,\pi^-)\mu^+\mu^-$ decays*, Phys. Rev. **D101** (2020) 035023, arXiv:1912.05811.

[25] LHCb collaboration, R. Aaij *et al.*, *Observation of the decay $\Lambda_b^0 \to pK^-\mu^+\mu^-$ and search for CP violation*, JHEP **06** (2017) 108, arXiv:1703.00256.

[26] LHCb collaboration, R. Aaij *et al.*, *Test of lepton universality using $\Lambda_b^0 \to pK^-\ell^+\ell^-$ decays*, JHEP **05** (2020) 040, arXiv:1912.08139.

[27] A. V. Sarantsev *et al.*, *Hyperon II: Properties of excited hyperons*, Eur. Phys. J. **A55** (2019) 180, arXiv:1907.13387.

[28] S. Meinel and G. Rendon, *$\Lambda_b^0 \to \Lambda^*(1520)\ell^+\ell^-$ form factors from lattice QCD*, Phys. Rev. **D103** (2021) 074505, arXiv:2009.09313.

[29] Particle Data Group, R. L. Workman *et al.*, *Review of particle physics*, Prog. Theor. Exp. Phys. **2022** (2022) 083C01.

[30] LHCb collaboration, A. A. Alves Jr. *et al.*, *The LHCb detector at the LHC*, JINST **3** (2008) S08005.

[31] LHCb collaboration, R. Aaij *et al.*, *LHCb detector performance*, Int. J. Mod. Phys. **A30** (2015) 1530022, arXiv:1412.6352.

[32] R. Aaij *et al.*, *The LHCb trigger and its performance in 2011*, JINST **8** (2013) P04022, arXiv:1211.3055.

[33] R. Aaij *et al.*, *Design and performance of the LHCb trigger and full real-time reconstruction in Run 2 of the LHC*, JINST **14** (2019) P04013, arXiv:1812.10790.

[34] F. Archilli *et al.*, *Performance of the muon identification at LHCb*, JINST **8** (2013) P10020, arXiv:1306.0249.

[35] T. Sjöstrand, S. Mrenna, and P. Skands, *A brief introduction to PYTHIA 8.1*, Comput. Phys. Commun. **178** (2008) 852, arXiv:0710.3820; T. Sjöstrand, S. Mrenna, and P. Skands, *PYTHIA 6.4 physics and manual*, JHEP **05** (2006) 026, arXiv:hep-ph/0603175.

[36] I. Belyaev *et al.*, *Handling of the generation of primary events in Gauss, the LHCb simulation framework*, J. Phys. Conf. Ser. **331** (2011) 032047.

[37] D. J. Lange, *The EvtGen particle decay simulation package*, Nucl. Instrum. Meth. **A462** (2001) 152.

[38] P. Golonka and Z. Was, *PHOTOS Monte Carlo: A precision tool for QED corrections in Z and W decays*, Eur. Phys. J. **C45** (2006) 97, arXiv:hep-ph/0506026.

[39] Geant4 collaboration, J. Allison *et al.*, *Geant4 developments and applications*, IEEE Trans. Nucl. Sci. **53** (2006) 270; Geant4 collaboration, S. Agostinelli *et al.*, *Geant4: A simulation toolkit*, Nucl. Instrum. Meth. **A506** (2003) 250.

[40] M. Clemencic *et al.*, *The LHCb simulation application, Gauss: Design, evolution and experience*, J. Phys. Conf. Ser. **331** (2011) 032023.

[41] LHCb collaboration, R. Aaij *et al.*, *Observation of $J/\psi p$ resonances consistent with pentaquark states in $\Lambda_b^0 \to J/\psi p K^-$ decays*, Phys. Rev. Lett. **115** (2015) 072001, arXiv:1507.03414.

[42] L. Breiman, J. H. Friedman, R. A. Olshen, and C. J. Stone, *Classification and regression trees*, Wadsworth international group, Belmont, California, USA, 1984.

[43] B. P. Roe *et al.*, *Boosted decision trees, an alternative to artificial neural networks*, Nucl. Instrum. Meth. **A543** (2005) 577, arXiv:physics/0408124.

[44] H. Voss, A. Hoecker, J. Stelzer, and F. Tegenfeldt, *TMVA - Toolkit for Multivariate Data Analysis with ROOT*, PoS **ACAT** (2007) 040.

[45] R. Aaij *et al.*, *Selection and processing of calibration samples to measure the particle identification performance of the LHCb experiment in Run 2*, Eur. Phys. J. Tech. Instr. **6** (2019) 1, arXiv:1803.00824.

[46] D. Martínez Santos and F. Dupertuis, *Mass distributions marginalized over per-event errors*, Nucl. Instrum. Meth. **A764** (2014) 150, arXiv:1312.5000.

[47] See supplemental material at [link inserted by publisher] for the additional figures.

[48] M. Pivk and F. R. Le Diberder, *sPlot: A statistical tool to unfold data distributions*, Nucl. Instrum. Meth. **A555** (2005) 356, arXiv:physics/0402083.

[49] Y. Xie, *sFit: a method for background subtraction in maximum likelihood fit*, arXiv:0905.0724.

[50] C. Langenbruch, *Parameter uncertainties in weighted unbinned maximum likelihood fits*, Eur. Phys. J. **C82** (2022) 393, arXiv:1911.01303.

[51] M. Hassanvand, S. Z. Kalantari, Y. Akaishi, and T. Yamazaki, *Theoretical analysis of* $\Lambda(1405) \to (\Sigma\pi)^0$ *mass spectra produced in* $p+p \to p+\Lambda(1405)+K^+$ *reactions*, Phys. Rev. **C87** (2013) 055202, Addendum ibid. **C88** (2013) 019905, arXiv:1210.7725.

[52] J. M. Blatt and V. F. Weisskopf, *Theoretical nuclear physics*, Springer, New York, 1952.

[53] T. Skwarnicki, *A study of the radiative cascade transitions between the Upsilon-prime and Upsilon resonances*, PhD thesis, Institute of Nuclear Physics, Krakow, 1986, DESY-F31-86-02.

[54] J. Smith, *The chebyshev function: Theory and applications*, Mathematical Review **42** (2010) 135.

[55] S. Descotes-Genon and M. Novoa-Brunet, *Angular analysis of the rare decay* $\Lambda_b \to \Lambda(1520)(\to N\bar{K})\ell^+\ell^-$, JHEP **06** (2019) 136, Erratum ibid. **06** (2020) 102, arXiv:1903.00448.

[56] Y.-S. Li, S.-P. Jin, J. Gao, and X. Liu, *The angular analysis of* $\Lambda_b \to \Lambda(1520)(\to N\bar{K})\ell^+\ell^-$ *decay*, arXiv:2210.04640.

[57] Y. Amhis, M. Bordone, and M. Reboud, *Dispersive analysis of* $\Lambda_b \to \Lambda(1520)$ *local form factors*, arXiv:2208.08937.

[58] S. Meinel and G. Rendon, $\Lambda_c \to \Lambda^*(1520)$ *form factors from lattice QCD and improved analysis of the* $\Lambda_b \to \Lambda^*(1520)$ *and* $\Lambda_b \to \Lambda_c^*(2595, 2625)$ *form factors*, Phys. Rev. **D105** (2022) 054511, arXiv:2107.13140.